Research Square

Preprints are preliminary reports that have not undergone peer review.
They should not be considered conclusive, used to inform clinical practice,
or referenced by the media as validated information.

A Flux-Constrained Generalized Finite Difference Method for Fractured Reservoir Simulation

Aaron Tellez
Khalifa University of Science and Technology
Aymen Laadhari
Khalifa University of Science and Technology
Hadi Hajibeygi
Delft University of Technology
Mohammed Al Kobaisi
mohammed.alkobaisi@ku.ac.ae

Khalifa University of Science and Technology

Research Article

Keywords:

Posted Date: November 9th, 2026

DOI: https://doi.org/10.21203/rs.3.rs-11335292/v1

License: This work is licensed under a Creative Commons Attribution 4.0 International License.
Read Full License

Additional Declarations: No competing interests reported.

A Flux-Constrained Generalized Finite Difference Method for Fractured Reservoir Simulation

Aaron Tellez[1], Aymen Laadhari[2], Hadi Hajibeygi[3], Mohammed Al Kobaisi[1*]

[1]Chemical and Petroleum Engineering Department, Khalifa University of Science and Technology, Abu Dhabi, 127788, United Arab Emirates.
[2]Department of Mathematics, Khalifa University of Science and Technology, Abu Dhabi, 127788, United Arab Emirates.
[3]Department of Geoscience and Engineering, Delft University of Technology, Delft, The Netherlands.

*Corresponding author(s). E-mail(s): mohammed.alkobaisi@ku.ac.ae;

Abstract

Meshless methods based on generalized finite difference formulations (GFDM) offer compelling advantages for reservoir simulation by eliminating global mesh generation and enabling arbitrary point placement. However, standard GFDM implementations fail to enforce local mass conservation. We develop a flux-constrained GFDM (FC-GFDM) that achieves local mass conservation through constrained meshless operators without sacrificing geometric flexibility, and extend it to fractured reservoirs via the embedded discrete fracture modeling (EDFM) framework. For each node, the method defines a local support domain and performs Delaunay triangulation within this region to construct control volumes as dual cells connecting circumcenters or centroids of sharing tetrahedra. This local construction requires no global mesh connectivity, enabling arbitrary point addition or removal without re-meshing. The perpendicular bisector (PEBI) nature of circumcenter-based dual cells provides natural orthogonality for efficient two-point flux approximations. Meshless operators are formulated through constrained Moving Least Squares where stencil coefficients simultaneously satisfy Taylor series consistency and discrete flux balance over the control volume. For matrix-fracture interaction, the method employs EDFM to represent fractures as 2D surfaces embedded within the 3D matrix point distribution. The rotation-invariant nature of meshless operators eliminates directional bias in coupling calculations and significantly simplifies handling of arbitrarily oriented and

intersecting fractures. Multi-point schemes addressing non-orthogonal geometries and full-tensor anisotropic permeability are presented. Numerical tests are carefully designed to showcase the conservation property and spatial discretization accuracy across irregular point distributions. The results indicate that our FC-GFDM can be practical for a diverse set of simulation problems.

Keywords: meshless methods, generalized finite differences, local mass conservation, embedded discrete fracture modeling, multipoint flux approximation

1 Introduction

The contemporary subsurface energy landscape is experiencing a fundamental transformation as the industry evolves from conventional hydrocarbon extraction to integrated subsurface energy resource management. This paradigm shift encompasses enhanced oil recovery (EOR) operations in massive mature fields, unconventional reservoir development, enhanced geothermal systems (EGS), and subsurface storage solutions for natural gas and hydrogen. Central to all these applications is the omnipresent influence of fracture networks, which fundamentally control fluid flow, storage capacity, and recovery efficiency, and present both challenges and opportunities whose complex and dynamic behavior across multiple scales and orientations demands advanced modeling capabilities.

The distinct paradigms of naturally fractured reservoir (NFR) simulation have evolved through three broad categories. Continuum approaches, from the Warren and Root double porosity model [1] and its Kazemi extension [2] to the Multiple Interacting Continua concept [3, 4], are computationally efficient but are limited by their inability to represent distinct large scale fractures and faults individually and by the inherent challenges in determining accurate shape factors. Discrete fracture network (DFN) models [5] address this by representing every fracture individually using unstructured finite volumes, but require the matrix mesh to conform to every fracture surface, producing excessively small grid cells near intersections and tips that make fracture conforming meshing prohibitively expensive at field scale. To overcome this meshing burden, Lee et al. [6] proposed a hierarchical approach in which long fractures are modeled explicitly as embedded fluid conduits connected to the matrix through non-neighboring connections (NNCs), with fracture and matrix discretizations generated independently, establishing what became the embedded discrete fracture modeling (EDFM) framework. Moinfar et al. [7] formalized this into a fully 3D compositional setting with NNC transmissibilities evaluated analytically from local geometry, without requiring the matrix mesh to conform to any fracture surface. Tçne et al. [8] further addressed the inaccuracy of EDFM for low conductivity fractures through the projection based pEDFM formulation, which modifies the local transmissibility stencil to correctly handle fractures across the full spectrum of conductivity contrasts.

The preferred attributes for the discretization of the flow equation, usually an elliptic partial differential equation (PDE), are local flux balance, flexibility, symmetric and positive definite discretization matrix, monotonicity, accuracy in fine and coarse

grids. Classical discretization candidates that target some of these attributes span several families: finite difference methods [9] approximate derivatives via truncated Taylor expansions on structured stencils, offering simplicity but failing on complex geometries and full tensor permeability; finite element methods [10] seek a weak solution over piecewise polynomial spaces on unstructured grids, but require postprocessing to recover local flux balance and lose accuracy at permeability discontinuities [11]; mixed and control volume finite element methods [12, 13] retain the first order flux conservation structure explicitly, improving accuracy at material interfaces at the cost of poor monotonicity and loss of symmetry. Finite volume methods (FVM) remain the de facto standard in industrial reservoir simulation [14], since they enforce local conservation directly by balancing fluxes across the faces of each control volume and accommodate diverse cell geometries. In its simplest and most widely used form, the two-point flux approximation, the flux across a face depends only on the two adjoining cell pressures; this is exact on K-orthogonal grids but loses consistency once the permeability becomes a full tensor or the grid turns non-K-orthogonal, leaving a grid orientation error that persists under refinement. The multipoint flux approximation (MPFA) was developed to lift this restriction: Aavatsmark et al. [15] introduced a control volume scheme for inhomogeneous, anisotropic media on non-K-orthogonal quadrilateral grids, and Edwards and Rogers [16] established the flux continuous formulation for the general tensor pressure equation, together rendering FVM consistent across a range of permeability tensors seen in practical problems. This combination of local conservation and geometric generality also makes FVM the natural host for EDFM, where it is routinely deployed on structured and unstructured grids. Yet, building conforming grids for complex reservoir geometries, irregular boundaries, and multiple intersecting fracture networks is a substantial burden, one that only grows in three-dimensional EDFM settings.

An alternative to the classical mesh based workflows are meshfree methods, which replace the globally connected mesh with a point cloud of nodes distributed either regularly or arbitrarily across the computational domain, whose coordinates alone constitute the spatial discretization. In this work, the generalized finite difference method (GFDM) is selected as the backbone for the meshfree framework. Introduced by Jensen [17] and further developed by Liszka and Orkisz [18] through a weighted least squares Taylor expansion, GFDM reconstructs differential operators at each node from a local influence domain of neighbors without any global mesh [19, 20]. Rao et al. [21, 22] demonstrated its practical viability for two phase porous flow and fractured reservoirs on regular point distributions, establishing that fractures can be discretized as independent lower dimensional point sets embedded in a 2D matrix cloud.

However, the most fundamental challenge for applying GFDM in reservoir simulation is the lack of local mass conservation. Conservation of mass and Dirac source/sink terms are imperative in transport solutions to avoid smeared saturation fronts and growing material balance errors. In GFDM, the transmissibility is computed locally at each node, where interface fluxes are not guaranteed to be equal and opposite. In consequence, conventional meshfree approaches are conservative only in limited cases where the point distribution is uniform, which stalls the widespread adoption of the method.

Hitherto, only limited attempts to enforce conservation in meshless settings have been made. Chiu et al. [23] enforced a volume weighted symmetry condition on the differential operator stencil coefficients, but was deemed computationally prohibitive for large and dynamic point clouds and inapplicable to irregular point clouds. Rao et al. [22] developed the Extended Finite Volume Method (EFVM), which uses virtual nodes to improve meshless operators' accuracy with a volume weighted condition on transmissibilities to recover local conservation. However, this condition only holds for large, symmetric, and regular distributed point clouds. Suchde et al. [24] extended conservation to asymmetric point clouds and higher order derivatives by enforcing a local discrete divergence theorem within the standard moving least squares framework to compute meshless operators. It uses monomial coefficients to ensure consistency and a weight function to address the overdetermined system under a two-point flux approximation scheme. Thus, the framework inherits the finite volume character of the flux, but also its consistency limitations for full permeability tensors and non-K-orthogonality.

In this work, we develop a novel flux-constrained generalized finite difference method (FC-GFDM), which enforces strict local mass conservation on meshless coefficients for arbitrary cloud points. The method augments the weighted least squares Taylor system with a Karush–Kuhn–Tucker (KKT) [25, 26] flux balance constraint derived from a finite volume stencil. A flux consistency identity proves that FC-GFDM recovers the target FV scheme satisfactorily. Moreover, we extend our method to fractured reservoirs via EDFM, with computed matrix–fracture NNC transmissibilities appended to the conservation balance without modifying the matrix stencil.

To our knowledge, this work is the first to formally address meshless local mass conservation for Eulerian frames in reservoir simulation.

The remainder of the paper is structured as follows. Section 2 presents the two phase flow and EDFM governing equations and the GFDM formulation. Section 3 develops the FC-GFDM framework: dual cell construction, KKT constrained operators, TPFA and MPFA-O variants, flux consistency proof, and EDFM coupling. Section 4 reports the numerical experiments and comparisons to the FV counterpart. Finally, some concluding remarks are outlined in Section 5.

2 Governing Equations and Meshless Formulation

2.1 Flow and Transport Equations

For a general two phase (oil–water) flow model in a single porosity matrix domain $\Omega \subset \mathbb{R}^n$, we assume isothermal conditions, Darcy flow, incompressible fluid phases and rock, and negligible capillary forces such that $p_o = p_w = p$ everywhere. The mass conservation equation for isothermal Darcy flow of phase $\alpha \in \{o, w\}$, neglecting gravity, is written as

$$\nabla \cdot \left(\frac{k\, k_{r\alpha}}{\mu_\alpha} \nabla p \right) + \bar{q}_\alpha = \frac{\partial}{\partial t}(\phi\, S_\alpha)\,, \qquad \Omega \subset \mathbb{R}^n, \tag{1}$$

where k denotes the absolute permeability, the material parameter of the porous medium, while $k_{r\alpha}(S_\alpha)$ is the saturation dependent relative permeability of phase α, μ_α the viscosity of phase α, p the pressure common to both phases, t the time, S_α the saturation of phase α, ϕ the reservoir porosity, and $\bar{q}_\alpha$ a volumetric source or sink term that can represent either a production well or an injection well. The formation volume factor is tacitly set to unity throughout, consistent with the incompressibility assumption.

Adding the respective phase mass equations and invoking the saturation constraint $S_w + S_o = 1$ at all times yields the pressure equation, which is elliptic by form:

$$\nabla \cdot \big(\lambda_w \, \nabla p + \lambda_o \, \nabla p\big) + q_t = 0, \tag{2}$$

where the phase mobilities are $\lambda_w = k\, k_{rw}(S_w)/\mu_w$ and $\lambda_o = k\, k_{ro}(S_w)/\mu_o$, with $k_{rw}(S_w)$ and $k_{ro}(S_w)$ functions of water saturation; the total mobility is $\lambda_t = \lambda_w + \lambda_o$ and the total source or sink is $q_t = \bar{q}_w + \bar{q}_o$.

The transport equation for the water phase saturation, hyperbolic in nature, is

$$\nabla \cdot \big(f_w(S_w)\, \mathbf{u}\big) + q_w = \phi \, \frac{\partial S_w}{\partial t}, \tag{3}$$

where the total Darcy velocity is $\mathbf{u} = \mathbf{u}_w + \mathbf{u}_o = -\lambda_t \, \nabla p$, the fractional flow of water is

$$f_w(S_w) = \frac{u_w}{u} = \frac{\lambda_w}{\lambda_w + \lambda_o}, \tag{4}$$

and q_w is the volumetric water source or sink.

Equation (2) computes the pressure and is referred to as the Flow equation, while Eq. (3) tracks the saturation S_w and is referred to as the Transport equation. The two equations are coupled in a sequential fully implicit (SFI) scheme: first Eq. (2) is solved for p, then $\mathbf{u} = -\lambda_t \nabla p$ is reconstructed and Eq. (3) is advanced for S_w, with the Jacobian updated after each outer iteration to provide strong coupling between the two subproblems. The fractional flow f_w is evaluated at the saturation of the upstream node based on the local flow direction—the upwind scheme—to stabilize the hyperbolic character of the Transport equation. Figure 1 shows the SFI solution loop.

2.2 EDFM Formulation

In the EDFM framework, fractures are represented as lower dimensional manifolds of dimension $(n-1)$ embedded in the n-dimensional matrix domain, and each medium is governed by its own conservation equation coupled through a volumetric exchange flux [6]. The matrix conservation equation for phase α is augmented by a matrix–fracture exchange term:

$$\nabla_m \cdot \left(\frac{k_m \, k_{r\alpha}}{\mu_\alpha} \, \nabla_m p_\alpha \right)_m + \bar{q}_\alpha + \bar{q}_{\alpha,mf} = \frac{\partial}{\partial t} (\phi \, S_\alpha)_m \,, \quad \Omega_m \subset \mathbb{R}^n, \tag{5}$$

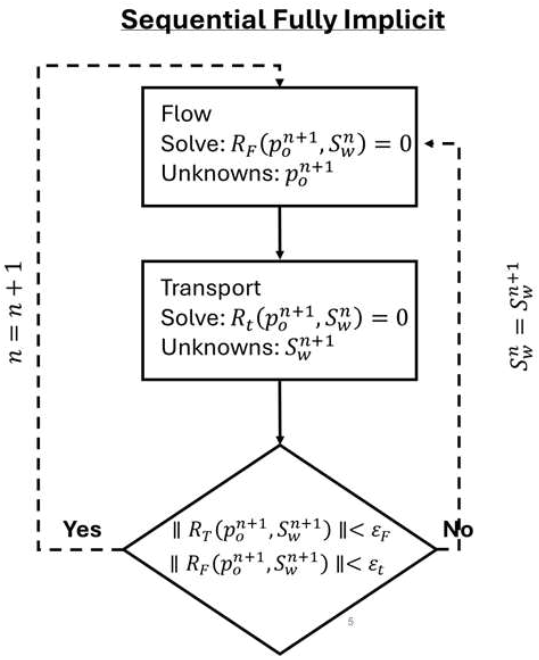


Fig. 1 Sequential fully implicit (SFI) solution scheme: the Flow and Transport equations are solved sequentially within each time step, with the Jacobian updated after every outer iteration until convergence.

where ∇_m denotes the divergent term in the matrix domain and $\bar{q}_{\alpha,mf}$ is the exchange flux per unit bulk volume (positive when flowing from matrix to fracture). The fracture conservation equation is

$$\nabla_f \cdot \left(\frac{k_f \, k_{r\alpha}}{\mu_\alpha} \nabla_f p_\alpha \right)_f + \bar{q}_\alpha - \bar{q}_{\alpha,mf} = \frac{\partial}{\partial t} (\phi \, S_\alpha)_f \,, \quad \Omega_f \subset \mathbb{R}^{n-1}, \tag{6}$$

where ∇_f is the $(n-1)$-dimensional gradient along the fracture manifold. The exchange term appears with opposite signs in Eqs. (5)–(6), ensuring global mass conservation between the two domains. Fracture–fracture intersections are handled through additional point source exchange terms inserted at the intersection nodes.

2.3 GFDM Formulation

A meshless discretization replaces the cell based connectivity of FVM with a set of N nodes $\{\mathbf{x}_i\}_{i=1}^N$ distributed over Ω, referred to collectively as the point cloud. The GFDM that underpins this framework builds its discrete operators from a weighted least squares Taylor fit over each local cloud [17–20]. No global mesh is constructed; the only spatial information used is the coordinate of each node. The domain is covered

by a collection of overlapping local influence domains $\{I_i\}_{i=1}^{N}$ such that

$$\Omega = \bigcup_{i=1}^{N} I_i, \qquad I_i \cap I_j \neq \emptyset, \tag{7}$$

where I_i denotes the set of nodes within a prescribed radius r_m of node i. The influence relationship is reciprocal: if $j \in I_i$ then $i \in I_j$. Each node $j \in I_i$ participates in the local approximation at node i, forming a local cloud of N_i neighbors used to reconstruct differential operators at $\mathbf{x}_i$. The radius r_m is chosen to include at least the minimum number of neighbors required for the desired polynomial basis: in two dimensions, five terms are needed (∂_x, ∂_y, ∂_{xx}, ∂_{yy}, ∂_{xy}), so the local system is overdetermined and the weighted least squares reconstruction is well conditioned. Figure 2 shows a representative local cloud, with the relative position vectors $\Delta\mathbf{x}_j = \mathbf{x}_j - \mathbf{x}_i$ that enter the Taylor reconstruction of the operators at $\mathbf{x}_i$.

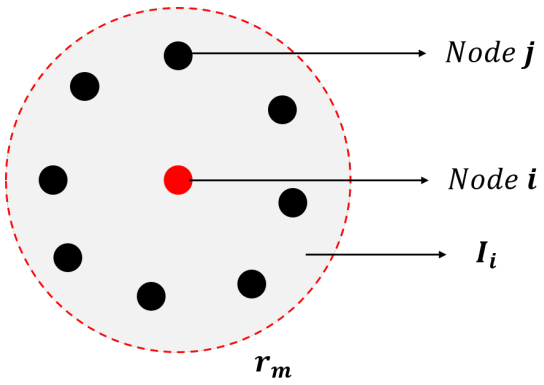


Fig. 2 Local support domain at node i: the central node (red) and its neighbors within the influence radius r_m (dashed).

For a fixed central node i, the value of a smooth function p at neighboring node $j \in I_i$ is expanded in a truncated Taylor series about $\mathbf{x}_i$:

$$\begin{aligned} p_j = p_i &+ \Delta x_j \frac{\partial p_i}{\partial x} + \Delta y_j \frac{\partial p_i}{\partial y} \\ &+ \frac{1}{2}\Big[\Delta x_j^2 \frac{\partial^2 p_i}{\partial x^2} + 2\,\Delta x_j\,\Delta y_j \frac{\partial^2 p_i}{\partial x \partial y} \\ &+ \Delta y_j^2 \frac{\partial^2 p_i}{\partial y^2}\Big] + O(h^2), \end{aligned} \tag{8}$$

where $\Delta x_j = x_j - x_i$, $\Delta y_j = y_j - y_i$, and $h = \|(\Delta x_j, \Delta y_j)\|$ is the characteristic spacing. Writing Eq. (8) for all N_i neighbors yields the overdetermined linear system

$$[X]\{Dp\} = \{P\}, \tag{9}$$

where the design matrix $[X] \in \mathbb{R}^{N_i \times 5}$, the pressure difference vector $\{P\} \in \mathbb{R}^{N_i}$, and the unknown derivative vector $\{Dp\} \in \mathbb{R}^5$ are

$$[X] = \begin{bmatrix} \Delta x_1 & \Delta y_1 & \frac{1}{2}\Delta x_1^2 & \frac{1}{2}\Delta y_1^2 & \Delta x_1 \Delta y_1 \\ \vdots & \vdots & \vdots & \vdots & \vdots \\ \Delta x_{N_i} & \Delta y_{N_i} & \frac{1}{2}\Delta x_{N_i}^2 & \frac{1}{2}\Delta y_{N_i}^2 & \Delta x_{N_i} \Delta y_{N_i} \end{bmatrix}, \tag{10}$$

$$\{P\} = \{p_1 - p_i,\ p_2 - p_i,\ \ldots,\ p_{N_i} - p_i\}^T, \textit{and} \tag{11}$$

$$\{Dp\}^T = \left\{ \frac{\partial p_i}{\partial x},\ \frac{\partial p_i}{\partial y},\ \frac{\partial^2 p_i}{\partial x^2},\ \frac{\partial^2 p_i}{\partial y^2},\ \frac{\partial^2 p_i}{\partial x \partial y} \right\}, \textit{respectively.} \tag{12}$$

Since $N_i > 5$ in general, the system is overdetermined and the optimal derivatives are found by minimizing the weighted least squares functional

$$B\big(\{Dp\}\big) = \big\| [W]^{1/2} \big(\{P\} - [X]\{Dp\} \big) \big\|^2, \tag{13}$$

where $[W] = \mathrm{diag}(w_1^2, \ldots, w_{N_i}^2) \in \mathbb{R}^{N_i \times N_i}$ is a diagonal weight matrix and each w_j penalizes distant neighbors according to [18, 19]

$$w_j = \begin{cases} 1 - 6\left(\dfrac{r_j}{r_m}\right)^2 + 8\left(\dfrac{r_j}{r_m}\right)^3 - 3\left(\dfrac{r_j}{r_m}\right)^4, & r_j \le r_m, \\ 0, & r_j > r_m, \end{cases} \tag{14}$$

with $r_j = \|\mathbf{x}_j - \mathbf{x}_i\|$. Setting $\partial B / \partial \{Dp\} = \mathbf{0}$ yields the 5×5 normal equations

$$[A]\{Dp\} = \{b\}, \qquad [A] = [X]^T [W][X], \quad \{b\} = [X]^T [W]\{P\}, \tag{15}$$

whose solution gives the meshless operator matrix

$$\{Dp\} = [M]\{P\}, \qquad [M] = [A]^{-1}[X]^T [W] \in \mathbb{R}^{5 \times N_i}. \tag{16}$$

The rows of $[M]$ contain the stencil coefficients for the five derivatives at node i. Denoting the (k, j) element of $[M]$ for central node i as m_{kj}^i, the explicit derivative approximations are

$$\left.\frac{\partial p}{\partial x}\right|_i = \sum_{j \in I_i} m_{1j}^i \, (p_j - p_i), \tag{17}$$

$$\left.\frac{\partial^2 p}{\partial x^2}\right|_i = \sum_{j \in I_i} m_{3j}^i \, (p_j - p_i), \tag{18}$$

$$\left.\frac{\partial^2 p}{\partial y^2}\right|_i = \sum_{j \in I_i} m_{4j}^i \, (p_j - p_i), \tag{19}$$

so that the discrete Laplacian at node i is

$$\Delta p\big|_i = \left.\frac{\partial^2 p}{\partial x^2}\right|_i + \left.\frac{\partial^2 p}{\partial y^2}\right|_i = \sum_{j\in I_i} \big(m_{3j}^i + m_{4j}^i\big)(p_j - p_i). \tag{20}$$

Substituting the GFDM Laplacian approximation Eq. (20) into the pressure equation (2) and evaluating pointwise at node i gives the standard meshless discrete pressure equation

$$\sum_{j\in I_i} \lambda_{t,ij}\, T_{ij}\, (p_j - p_i) + q_{t,i}\, V_i = 0, \tag{21}$$

where, integrating the Laplacian over the control volume V_i of node i, we define the GFDM transmissibility

$$T_{ij} = k_{ij}\, V_i \big(m_{3j}^i + m_{4j}^i\big), \tag{22}$$

k_{ij} is the interface harmonic mean permeability of k_i and k_j, $\lambda_{t,ij}$ is the total mobility evaluated at the interface, and $q_{t,i}$ is the total source or sink per unit volume at node i.

Although the GFDM formulation outlined above is locally consistent and geometrically flexible, it can, and often will, violate strict local mass conservation. This can be seen in the asymmetry of the GFDM transmissibility. The coefficient

$$T_{ij} = k_{ij}\, V_i\, (m_{3j}^i + m_{4j}^i) \tag{23}$$

is determined by the stencil at node i, while the reciprocal coefficient

$$T_{ji} = k_{ji}\, V_j\, (m_{3i}^j + m_{4i}^j) \tag{24}$$

is determined independently by the stencil at node j. Because the two stencils are constructed from different local neighborhoods with different weight matrices and different control volumes $V_i \neq V_j$, in general

$$T_{ij} \neq T_{ji}, \tag{25}$$

so the flux from i to j perceived by node i is not equal and opposite to the flux from j to i perceived by node j. In transport solutions the phase fluxes entering each node may be computed from the same asymmetric transmissibilities, so fractional amounts of mass appear or disappear at every interface at every time step. These local mass defects accumulate over time, producing errors in the saturation field and material balance errors that grow with the number of time steps and the severity of point cloud irregularity [24].

It is clear that GFDM enforces the PDE pointwise, without a discrete divergence theorem. As a consequence, the method is conservative only for uniform, symmetric point clouds. In order to achieve local conservation of mass and keep track of the saturation front, information of the local divergence operator must be provided. For a conservation law $\nabla \cdot \mathbf{u} = q$ with $\mathbf{u} = -\lambda \nabla p$, integrating over any control cell Ω_i and

applying the divergence theorem gives the integral balance

$$\int_{\partial\Omega_i} \lambda \nabla p \cdot \hat{\mathbf{n}}\, dA + \int_{\Omega_i} q\, dV = 0. \tag{26}$$

Finite volume methods enforce a local discrete version of (26) on each control cell, whereas GFDM satisfies only the pointwise strong form. The lack of conservation undermines the primary motivation for adopting a meshless framework for arbitrary cloud points in different domains. The flux-constrained formulation developed in Section 3 directly addresses this limitation by modifying the stencil construction to enforce local conservation as a constraint inside the weighted least squares framework at each node, and thereby recovering the integral balance.

3 Flux-Constrained GFDM Formulation

The flux-constrained GFDM (FC-GFDM) enforces strict local mass conservation by augmenting the weighted least squares system at each node with a constraint that forces the discrete divergence operator to reproduce a prescribed finite volume flux identity over its selected influence nodes. Following the ideas of earlier conservative meshless schemes [23], and more recently the works of Suchde et al., we develop a FC-GFDM formulation that recovers strict local conservation on nonsymmetric, arbitrary point clouds and remains consistent for full tensor material parameters.

The framework is presented in the following four subsections. Section 3.1 constructs a local dual cell at each node to provide geometric information of control volumes V_i, interface areas A_{il}, and normals $\hat{\mathbf{n}}_{il}$, and presented in two modes: PEBI and centroid. Unlike Finite Volume Methods, we note here that the notion of a mesh is merely for local balances and not based on a predefined global mesh; the discretization in itself remains entirely meshless. The fundamental structure of the flux conservation constraint is given in Section 3.2. Section 3.3 conditions the constraint to give a TPFA-like or MPFA-O-like flux stencil, and Section 3.4 presents the formulation for fractured media via EDFM.

3.1 Local Dual Cells

The development of Local Dual Cells targets the premise that the discretization remains valid for arbitrary and asymmetric point clouds and requires no global remeshing. The goal here is to generate geometric quantities for the constraint optimization (discussed next in Section 3.2), which is robust and can also be used for adaptive/dynamic remeshing applications such as fracture propagation modeling. A volume cell is generated locally at each node as a combination of two dual Delaunay triangles around its support nodes. This tessellation can be created in two ways, in centroid and PEBI modes, each providing a polygon, or a polyhedron in 3D, with distinct geometric characteristics.

Starting from a support set I_i, local Delaunay triangulation is formed; the triangles incident to node $\mathbf{x}_i$ identify the geometric neighbors $\mathcal{N}(i)$, and the dual vertices of

these triangles, depending on the tessellation choice, are connected to the control cell Ω_i of volume V_i.

For each node $\mathbf{x}_i$, let $\mathcal{T}_i$ be the Delaunay triangulation of the support set $I_i = \{\mathbf{x}_j : \|\mathbf{x}_j - \mathbf{x}_i\| \leq r_m\}$. From $\mathcal{T}_i$, we keep the triangles incident to $\mathbf{x}_i$,

$$\mathcal{T}_i^* = \big\{t \in \mathcal{T}_i : \mathbf{x}_i \in t\big\}, \qquad r_m = \beta h, \tag{27}$$

where r_m is the radius of support multiplied by the characteristic spacing h introduced in Section 2.3, β controls the neighbor count, and $|I_i| \approx \pi\beta^2$. Suchde [27] recommends $1.8 \leq \beta \leq 2.5$.

The dual cell Ω_i is a polygon whose vertices are geometric points derived from the combination of two triangles $t \in \mathcal{T}_i^*$. As mentioned before, two choices of dual cells are possible depending on the vertex construction mode:

$$\mathbf{v}_t = \begin{cases} \mathbf{c}_t, & \text{PEBI / circumcenter mode,} \\ \bar{\mathbf{x}}_t = \frac{1}{3}\sum_{k\in t}\mathbf{x}_k, & \text{centroid (barycentric) mode,} \end{cases} \tag{28}$$

where $\mathbf{v}_t$ is the dual vertex contributed by triangle t, $\mathbf{c}_t$ is its circumcenter and $\bar{\mathbf{x}}_t$ the centroid of triangle t.

In PEBI grids, when $\mathbf{v}_t = \mathbf{c}_t$, the polygon Ω_i coincides with the cell of $\mathbf{x}_i$ in the Delaunay diagram, i.e. the set of points closer to $\mathbf{x}_i$ than to any other node. The key geometric property is that the segment $\mathbf{x}_i\mathbf{x}_l$ is perpendicular to the shared interface $\Gamma_{il} = \Omega_i \cap \Omega_l$ on each point cloud. This orthogonality makes the grid suitable for TPFA flux approximations (31). Moreover, this mode is a natural choice when the point distribution is regular or slightly irregular. Figure 3 shows the steps to construct the dual cells for interior, edge, and corner nodes with the circumcenter taken as the dual vertices.

In centroid mode, also known as the barycentric method, setting $\mathbf{v}_t = \bar{\mathbf{x}}_t$ creates the polygon Ω_i. This choice guarantees that the dual cell is always a convex polygon, independent of the point cloud regularity. The centroid mode creates a robust cell on highly irregular clouds or near sharp domain boundaries where circumcenters may fall outside the domain. For this case, the TPFA is no longer valid and an MPFA-O method is sought instead. Figure 4 shows the construction of dual cells for interior, edge, and corner nodes with the centroid taken as the dual vertices.

Each node builds its own dual cell on its own support, so the interface Γ_{il} between two cells, with area A_{il} and outward normal $\hat{\mathbf{n}}_{il}$, is defined twice, once from node i and once from node l, and the two definitions may not coincide. The discrepancy between these node local interface definitions is quantified by the nonstitch error

$$\varepsilon_{\text{mesh}} = \frac{\displaystyle\sum_i \sum_{l\in\mathcal{N}(i)} \left\|\hat{\mathbf{n}}_{il}A_{il} + \hat{\mathbf{n}}_{li}A_{li}\right\|}{2\displaystyle\sum_i V_i}, \tag{29}$$

which is zero for a global tessellation and positive for local dual cells, decreasing as the support radius grows, where $\hat{\mathbf{n}}_{li} = \mathbf{0}$ and $A_{li} = 0$ whenever $i \notin \mathcal{N}(l)$. Because each

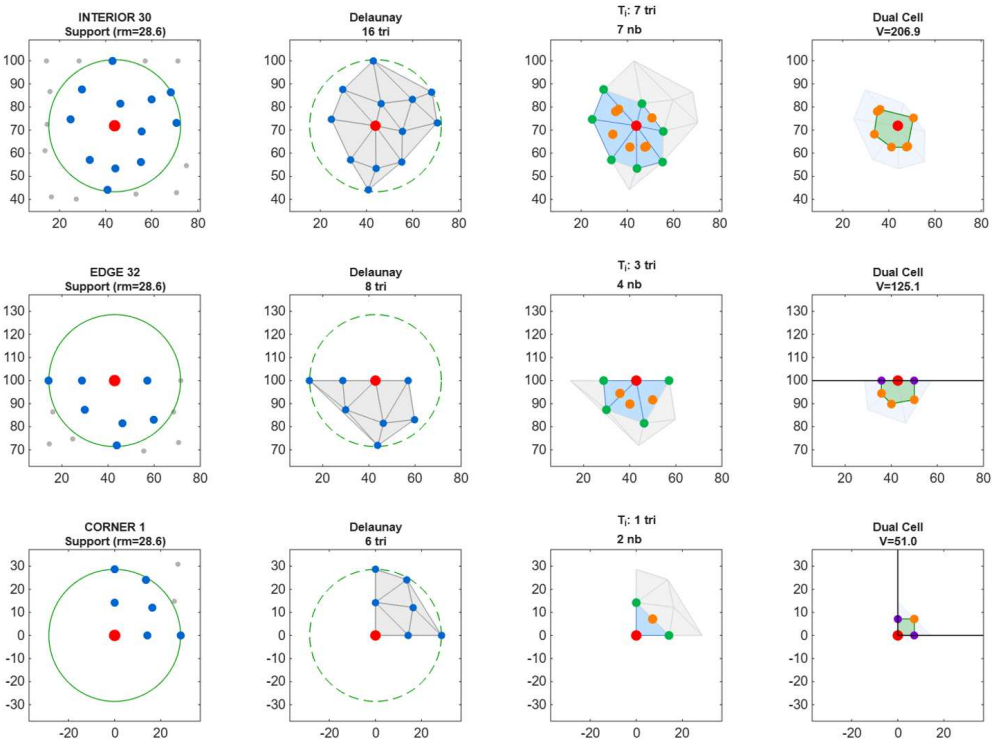


Fig. 3 PEBI (circumcenter) dual cell construction for interior, edge, and corner nodes.

dual cell is built locally on its own support domain rather than from a global mesh, adjacent cells need not stitch into a consistent global tiling. On a global tessellation $\hat{\mathbf{n}}_{il}A_{il} = -\hat{\mathbf{n}}_{li}A_{li}$ for every pair, so the interface contributions cancel and $\varepsilon_{\text{mesh}} = 0$, whereas small supports with too few neighbors yield nonsymmetric adjacent cells ($A_{il} \neq A_{li}$, $\hat{\mathbf{n}}_{il} \neq -\hat{\mathbf{n}}_{li}$) and $\varepsilon_{\text{mesh}} > 0$. By the uniqueness of the Delaunay tessellation, enlarging the support radius restores the stitching and drives $\varepsilon_{\text{mesh}}$ toward zero [27]. A larger support radius is therefore beneficial for the stitching.

Figure 5 contrasts the resulting tessellations over the full domain in the two modes. Both partitions are built from the same node set and differ only in the dual vertex rule, the PEBI interfaces lying orthogonal to the internode segments while the centroidal cells remain well defined for any triangle shape.

3.2 Flux Conservation Constraint

Building on the standard GFDM operators established in Section 2.3, we now develop the FC-GFDM equations. Starting from the elliptic pressure equation (2), we integrate over the control volume Ω_i of node i and apply the divergence theorem (26) to the flux part, discretizing the surface integral as a sum of fluxes across the dual cell interfaces.

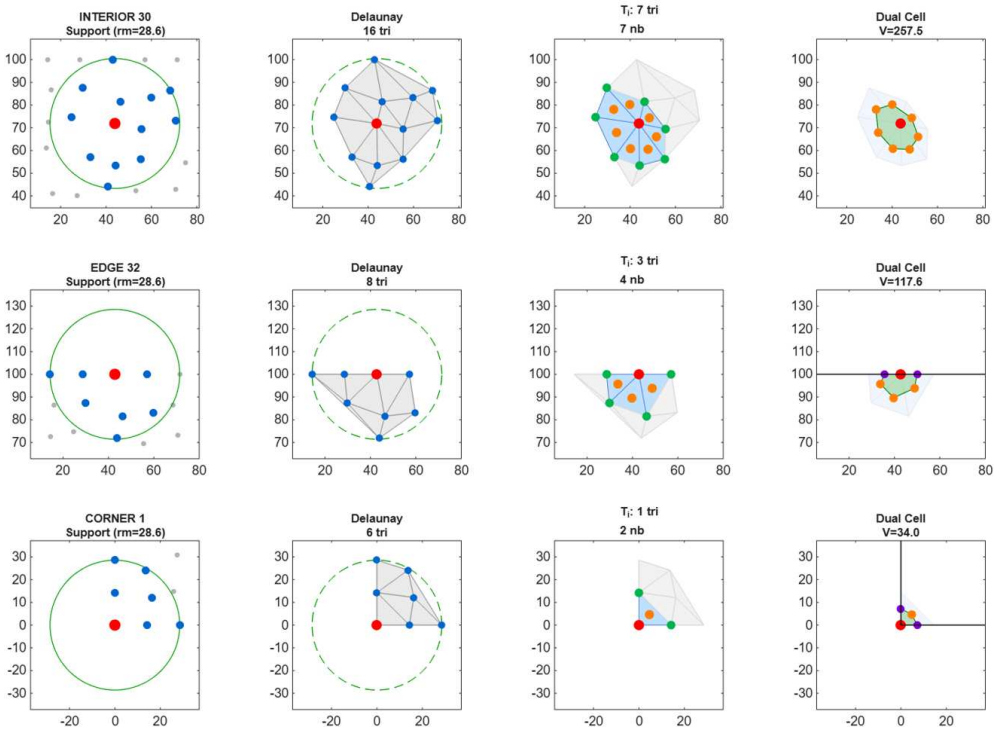


Fig. 4 Centroid (barycentric) dual cell construction for an interior node (top), an edge node (middle), and a corner node (bottom).

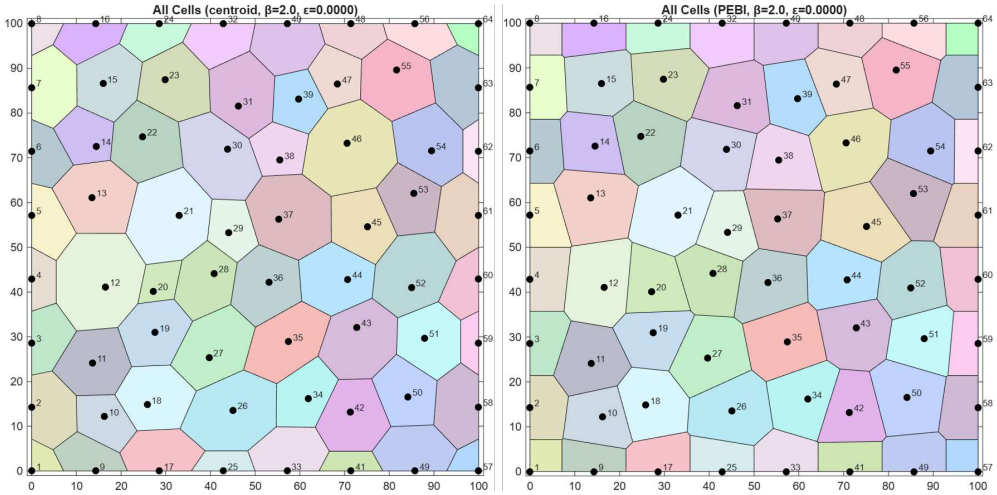


Fig. 5 Dual cell tessellation of the full domain for a regular point cloud ($\beta = 2.0$, $\varepsilon = 0$): centroid mode (left) and PEBI mode (right). The centroidal cells are compact and convex, whereas the PEBI cells recover the orthogonal Voronoi partition.

This yields the control volume balance

$$V_i\,\partial_i^D p = \sum_{l\in\mathcal{N}(i)} F_{il}(\lambda_{il}, p), \tag{30}$$

where V_i is the volume of the dual cell Ω_i, $\partial_i^D p$ the discrete divergence at node i, $\mathcal{N}(i)$ the geometric neighbors of node i, and F_{il} the flux across the dual interface Γ_{il}. The TPFA approximation is given by

$$F_{il}(\lambda_{il}, p) = \lambda_{il}\,A_{il}\,(\hat{\mathbf{n}}_{il}\cdot\hat{\mathbf{e}}_{il})\,\frac{p_l - p_i}{d_{il}}, \qquad \hat{\mathbf{e}}_{il} = \frac{\mathbf{x}_l - \mathbf{x}_i}{d_{il}}, \tag{31}$$

where λ_{il} is the harmonically averaged mobility, A_{il} the area of the dual interface Γ_{il}, $\hat{\mathbf{n}}_{il}$ its outward unit normal, $\hat{\mathbf{e}}_{il}$ the unit vector along the line joining nodes i and l formed from the node coordinates $\mathbf{x}_i$, and $d_{il} = \|\mathbf{x}_l - \mathbf{x}_i\|$ the internode distance. Note that the cosine $\hat{\mathbf{n}}_{il}\cdot\hat{\mathbf{e}}_{il}$ equals unity for orthogonal meshes.

The flux-constrained operator replaces the unconstrained GFDM divergence stencil of Eq. (20) by coefficients that approximate the discrete divergence at node i while enforcing conservation. These coefficients satisfy three requirements: (i) consistency: from the Taylor series (8), the stencil reproduces the divergence operator,

$$\sum_{j\in\mathcal{S}(i)} m_{ij}^{\mathrm{FC}}\,\mathbf{t}_{ij} = \mathbf{c}^{TPFA}, \tag{32}$$

(ii) flux conservation at the current time level n,

$$\sum_{j\in\mathcal{S}(i)} m_{ij}^{\mathrm{FC}}\,p_j^{(n)} = \frac{1}{V_i}\sum_{l\in\mathcal{N}(i)} F_{il}(\lambda_{il}, p^{(n)}); \tag{33}$$

(iii) minimum weighted norm,

$$\min \sum_{j\in\mathcal{S}(i)} \left(\frac{m_{ij}^{\mathrm{FC}}}{w_j}\right)^2, \tag{34}$$

where m_{ij}^{FC} are the flux-constrained meshless coefficients of node i over its stencil support $\mathcal{S}(i)$, $\mathbf{t}_{ij} = (\Delta x_j,\ \Delta y_j,\ \frac{1}{2}\Delta x_j^2,\ \frac{1}{2}\Delta y_j^2,\ \Delta x_j\,\Delta y_j)^T$ is the vector of Taylor series coefficients of neighbor j in Eq. (8) (row j of the design matrix $[X_i]$ of Eq. (10)), $p_j^{(n)}$ is the pressure at time level n, and $w_j = W(r_j)$ is the same distance weight used in the GFDM reconstruction, Eq. (14). The consistency condition (32) together with the flux conservation condition (33) leaves the stencil coefficients underdetermined, and the minimum weighted norm objective (34) gives a unique solution.

Substituting Eq. (31) into Eq. (33) gives

$$C_{\text{flux}}(j) = \begin{cases} +\dfrac{\lambda_{il}\, A_{il}\, (\hat{\mathbf{n}}_{il} \cdot \hat{\mathbf{e}}_{il})}{d_{il}\, V_i} & j \in \mathcal{N}(i), \\ -\displaystyle\sum_{l \in \mathcal{N}(i)} \dfrac{\lambda_{il}\, A_{il}\, (\hat{\mathbf{n}}_{il} \cdot \hat{\mathbf{e}}_{il})}{d_{il}\, V_i} & j = i, \\ 0 & \text{otherwise}, \end{cases} \tag{35}$$

where $C_{\text{flux}}(j)$ is the two-point flux coefficient that the TPFA approximation prescribes for neighbor j; it is the TPFA realization of the general constraint target g_j introduced below. The constraint Eq. (33) is satisfied when $m_{ij}^{\text{FC}} = C_{\text{flux}}(j)$ for all j.

The flux conservation constraint (33) is encoded as a linear condition on the operator matrix,

$$\mathbf{c}^T [M_i] = \mathbf{g}_j^T, \tag{36}$$

where $[M_i] \in \mathbb{R}^{5 \times N_i}$ is the unconstrained meshless operator matrix, $\mathbf{c} \in \mathbb{R}^5$ the constraint direction aligned with the chosen divergence operator, and $\mathbf{g}_j = (g_1, \ldots, g_{N_i})^T$ the prescribed finite volume target, scheme independent in that each flux variant supplies its own entries g_j. In the two-point case, $g_j = C_{\text{flux}}(j)$ of Eq. (35) and is a per-face flux coefficient with the Laplacian direction $\mathbf{c}^{TPFA} = [0, 0, 1, 1, 0]^T$; in the multipoint case, $g_j = g_j^{MPFA-O}$ and is an assembled target over the support $\mathcal{S}(i)$, with full tensor direction $\mathbf{c}^{MPFA-O}$ given in Section 3.3. We thus reserve C_{flux} for the TPFA face flux and g_j for the general target.

Now, the minimization problem of Eq. (34) is solved by the first order KKT conditions [25, 26], which apply a Lagrange multiplier for the flux constraint to the weighted least squares system,

$$\underbrace{\begin{bmatrix} [A_i] & \mathbf{c} \\ \mathbf{c}^T & 0 \end{bmatrix}}_{[K_i] \in \mathbb{R}^{6 \times 6}} \begin{pmatrix} \mathbf{m}_j^i \\ \mu_j \end{pmatrix} = \begin{pmatrix} [X_i]^T [W_i] \mathbf{e}_j \\ g_j \end{pmatrix}, \tag{37}$$

where $[K_i] \in \mathbb{R}^{6 \times 6}$ is the KKT matrix, $[A_i] = [X_i]^T [W_i] [X_i] \in \mathbb{R}^{5 \times 5}$ is the weighted matrix of Eq. (15), assembled from the Taylor design matrix (10) and the weights (14), $\mathbf{m}_j^i \in \mathbb{R}^5$ is the j-th column of the operator (the derivative coefficients tied to neighbor j), $\mathbf{e}_j$ is the j-th basis vector of $\mathbb{R}^{N_i}$, g_j is the corresponding entry of $\mathbf{g}_j$, and μ_j is the Lagrange multiplier enforcing the flux balance.

Because $[A_i]$ is symmetric positive definite whenever $[X_i]$ has full column rank, the KKT system (37) has a unique solution. Appendix A provides the elimination steps of the Lagrange multiplier by block elimination that yields the following structure of the flux-constrained meshless operator

$$\mathbf{m}_j^{i,\text{FC}} = \underbrace{[G_i^{\text{unc}}] \mathbf{e}_j}_{\text{unconstrained}} \underbrace{- \frac{1}{\gamma_i} [A_i]^{-1} \mathbf{c} \left(\mathbf{c}^T [G_i^{\text{unc}}] \mathbf{e}_j - g_j \right)}_{\text{FC constraint correction}}, \tag{38}$$

where $[G_i^{\mathrm{unc}}] = [A_i]^{-1}[X_i]^T[W_i]$ is the unconstrained part of the GFDM operator $[M]$ of Eq. (16) and $\gamma_i = \mathbf{c}^T[A_i]^{-1}\mathbf{c} > 0$. Solving (37) for all j simultaneously assembles the flux-constrained meshless operator matrix as

$$[M_i^{\mathrm{FC}}] \in \mathbb{R}^{5\times N_i}, \tag{39}$$

whose (k, j) entry is $m_{kj}^{i,\mathrm{FC}}$. The KKT matrix $[K_i]$ is nonsingular provided that $[A_i]$ is positive definite and $\mathbf{c} \notin \ker([A_i])$, which holds when $[X_i]$ has full column rank.

3.3 FC-GFDM Flux variants

The two-point flux approximation of Eq. (31) is not consistent if the permeability is a full tensor or the dual interfaces turn nonorthogonal, as they do on centroidal dual cells. Strictly speaking, TPFA is only valid when the co-normal $\boldsymbol{K}\hat{\mathbf{n}}_{il}$ is parallel to the internode line $\hat{\mathbf{e}}_{il}$, $|\boldsymbol{K}\hat{\mathbf{n}}_{il} \times \hat{\mathbf{e}}_{il}| = 0$. Multipoint flux approximation methods restore consistency through a vertex interaction region: they reconstruct the pressure gradient from surrounding cell pressures and enforce flux continuity at each subinterface. As a result, the internode flux becomes a multipoint expression that captures the transverse contribution and keeps the transmissibility terms consistent for full permeability tensors and nonorthogonal grids [16, 28].

Here, we adopt the MPFA-O method. Around each vertex O shared by cells $\Omega_1, \Omega_2, \Omega_3, \Omega_4$ (ordered counterclockwise), the interaction region is formed by connecting each cell centre $\mathbf{x}_k$ to the midpoints A, B, C, D of the faces of Ω_k incident to O. This produces four triangular subregions $\triangle_1 = (\mathbf{x}_1, A, D)$, $\triangle_2 = (\mathbf{x}_2, A, B)$, $\triangle_3 = (\mathbf{x}_3, B, C)$, $\triangle_4 = (\mathbf{x}_4, C, D)$ and four subinterfaces OA, OB, OC, OD through which the local fluxes are computed, as shown in Fig. 6.

Inside subregion $\triangle_1$ the pressure is assumed linear, giving a constant gradient

$$\nabla p\big|_{\triangle_1} = \frac{1}{2|\triangle_1|}\big[\boldsymbol{\nu}_{1,A}(p_A - p_1) + \boldsymbol{\nu}_{1,D}(p_D - p_1)\big], \tag{40}$$

where $|\triangle_1|$ is the area of subregion $\triangle_1$, p_1 the pressure at cell centre $\mathbf{x}_1$, p_A and p_D the auxiliary midpoint pressures of Fig. 6 bounding $\triangle_1$, and $\boldsymbol{\nu}_{k,m}$ the inward normal of $\triangle_k$ to the edge opposite vertex m, with magnitude equal to the edge length. Through these inward normals and the auxiliary midpoint pressures, the reconstruction retains the transverse component of the gradient that the two-point stencil ignores. The flux through subinterface OA from the $\triangle_1$ side is

$$f_A^{(1)} = -\mathbf{n}_A^T\,\boldsymbol{K}_1\,\nabla p\big|_{\triangle_1} = \omega_{A,1,A}\,(p_A - p_1) + \omega_{A,1,D}\,(p_D - p_1), \tag{41}$$

where the transmissibility building block is [28]

$$\omega_{\alpha,k,m} = -\frac{\mathbf{n}_\alpha^T\,\boldsymbol{K}_k\,\boldsymbol{\nu}_{k,m}}{2|\triangle_k|}, \tag{42}$$

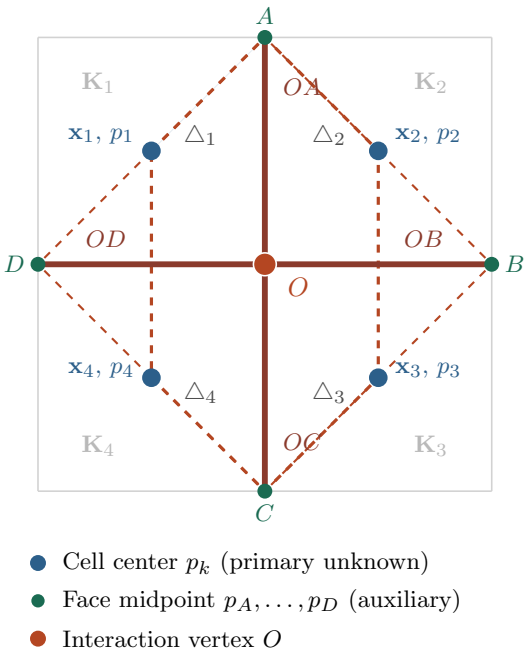


Fig. 6 Interaction region around vertex O. Subregions $\triangle_1$–$\triangle_4$ connect each cell centre to its two adjacent face midpoints. Subinterfaces OA–OD (solid) carry the local fluxes; the dashed boundary outlines the full interaction region.

with $\mathbf{n}_\alpha$ the outward normal to subinterface α and $\boldsymbol{K}_k$ the permeability tensor of cell Ω_k. Imposing flux continuity at each subinterface yields four equations in the auxiliary pressures $\bar{\mathbf{p}} = (p_A, p_B, p_C, p_D)^T$ and collected as

$$\mathbf{A}\,\bar{\mathbf{p}} = \mathbf{B}\,\mathbf{p}, \tag{43}$$

where the entries of $\mathbf{A}$ and $\mathbf{B}$ are sums of ω-coefficients from the two subregions sharing each subinterface, and $\mathbf{p} = (p_1, p_2, p_3, p_4)^T$ collects the four cell pressures. Substituting into the one sided flux expressions $\mathbf{f} = \mathbf{C}\bar{\mathbf{p}} + \mathbf{D}\mathbf{p}$, where $\mathbf{f} = (f_A, f_B, f_C, f_D)^T$ is the subinterface flux vector and $\mathbf{C}, \mathbf{D}$ likewise collect the ω-coefficients, gives

$$\mathbf{f} = \underbrace{\left(\mathbf{C}\,\mathbf{A}^{-1}\mathbf{B} + \mathbf{D}\right)}_{\mathbf{T}}\,\mathbf{p}, \tag{44}$$

where $\mathbf{T}$ is the 4×4 dense transmissibility matrix. Accumulating these local transmissibilities over all interaction regions assembles the global cell centered MPFA-O stencil

$$\sum_{j \in \mathcal{S}(i)} T_{ij}^{MPFA-O}\, p_j \approx V_i\, \nabla\cdot(\boldsymbol{\Lambda}\nabla p)\big|_i, \tag{45}$$

whose assembled coefficient T_{ij}^{MPFA-O} links nodes i and j and approximates the full tensor divergence $\nabla\cdot(\boldsymbol{\Lambda}\nabla p)$ of the mobility tensor $\boldsymbol{\Lambda} = \boldsymbol{K}/\mu$, with μ being the

fluid viscosity. Inserting the assembled MPFA-O flux (45) into the flux conservation constraint (33) yields the multipoint target vector

$$g_j^{MPFA-O} = \begin{cases} +\dfrac{1}{V_i} \displaystyle\sum_{l \in \mathcal{N}(i)} t_{il,j} & j \in \mathcal{S}(i) \setminus \{i\}, \\ -\dfrac{1}{V_i} \displaystyle\sum_{l \in \mathcal{N}(i)} \sum_{m \neq i} t_{il,m} & j = i, \\ 0 & \text{otherwise.} \end{cases} \tag{46}$$

As in the TPFA case, the same KKT system described by (37) is used here; only the constraint direction $\mathbf{c}$ and the target $\mathbf{g}_j$ change. For the MPFA-O variant the direction $\mathbf{c}^{MPFA-O}$ is chosen for the full tensor divergence $\nabla \cdot (\boldsymbol{\Lambda} \nabla p)$ of the mobility tensor $\boldsymbol{\Lambda} = \boldsymbol{K}/\mu$ and the target is the multipoint vector $\mathbf{g}_j^{MPFA-O}$ of Eq. (46), resulting in the constrained meshless operator $m_{ij}^{\mathrm{FC},MPFA-O}$, whereas for the FC-GFDM–TPFA variant, $\mathbf{c}^{TPFA}$ is chosen for the Laplacian $\nabla^2 p$ with target $g_j^{TPFA} = C_{\mathrm{flux}}(j)$ of Eq. (35). From the flux-constrained matrix $[M_i^{\mathrm{FC}}]$, the discrete divergence at node i is

$$\partial_i^D p = \sum_{j \in I_i} \lambda_{ij} \left(\mathbf{c}^T \mathbf{m}_j^{i,\mathrm{FC}}\right)(p_j - p_i) = \sum_{j \in I_i} \lambda_{ij}\, m_{ij}^{\mathrm{FC}}\, (p_j - p_i), \tag{47}$$

where $\mathbf{m}_j^{i,\mathrm{FC}}$ is the j-th column of $[M_i^{\mathrm{FC}}]$ and $m_{ij}^{\mathrm{FC}} = \mathbf{c}^T \mathbf{m}_j^{i,\mathrm{FC}}$ is the flux-constrained meshless operator: for a 2D case, with $\mathbf{c} = \mathbf{c}^{TPFA}$ it reduces to the Laplacian $m_{3j}^{i,\mathrm{FC}} + m_{4j}^{i,\mathrm{FC}}$, and with $\mathbf{c} = \mathbf{c}^{MPFA-O}$ it gives the full tensor combination $\Lambda_{xx} m_{3j}^{i,\mathrm{FC}} + \Lambda_{yy} m_{4j}^{i,\mathrm{FC}} + 2\Lambda_{xy} m_{5j}^{i,\mathrm{FC}}$.

To solve the system in a sequential fully implicit mode, as highlighted in Fig. 1, we now cast the flow and transport equations in their residual forms. For flow,

$$\mathcal{R}_i^p(p^{n+1}, S_w^{n+1}) = V_i\, \partial_i^D p^{n+1} + q_{t,i}\, V_i = 0, \tag{48}$$

where $\mathcal{R}_i^p$ is the pressure residual at node i, V_i the dual cell volume, $\partial_i^D p^{n+1}$ is the flux-constrained discrete divergence, $q_{t,i}$ the total source or sink per unit volume, and the superscript $n+1$ refers to the new time level. The conservative fluxes follow from the same stencil,

$$F_{ij}^{n+1} = \lambda_{ij}\, V_i\, m_{ij}^{\mathrm{FC}}\, (p_j^{n+1} - p_i^{n+1}), \tag{49}$$

where F_{ij}^{n+1} is the conservative internode flux at the new time level, λ_{ij} the interface total mobility carrying the permeability tensor $\boldsymbol{K}$, m_{ij}^{FC} the flux-constrained meshless operator, and p_i^{n+1}, p_j^{n+1} the nodal pressures at the new time level. And for transport,

$$\mathcal{R}_i^w(p^{n+1}, S_w^{n+1}) = \phi_i\, V_i\, \frac{S_{w,i}^{n+1} - S_{w,i}^n}{\Delta t} - \sum_j f_{w,ij}^{\mathrm{up}}\, F_{ij}^{n+1} - q_{w,i} = 0, \tag{50}$$

where $\mathcal{R}_i^w$ is the transport residual at node i, ϕ_i is the porosity, $S_{w,i}^{n+1}$ and $S_{w,i}^n$ are the water saturations at the new and old time levels, Δt is the time step, $f_{w,ij}^{\mathrm{up}}$ is the

Algorithm 1 FC-GFDM pressure solver

Require: point cloud $\{\mathbf{x}_i\}_{i=1}^{N}$, permeability $\boldsymbol{K}$, support parameter β, saturation $\{S_w\}$
Ensure: pressure $\{p^{n+1}\}$

for $i = 1$ **to** N **do**
  support I_i and weighted matrix $[A_i] = [X_i]^T[W_i][X_i]$
  dual cell Ω_i by PEBI/centroid node selection: V_i, $\mathcal{N}(i)$, A_{il}, $\hat{\mathbf{n}}_{il}$ ▷ Section 3.1
  interface mobilities λ_{il} from $\{S_w\}$
  if Ω_i face-orthogonal **and** $\boldsymbol{K}$ isotropic **then**
    $\mathbf{c} \leftarrow \mathbf{c}^{TPFA}$, $\mathbf{g}_j \leftarrow \{C_{\text{flux}}(j)\}$
  else
    $\mathbf{c} \leftarrow \mathbf{c}^{MPFA-O}$, $\mathbf{g}_j \leftarrow \mathbf{g}_j^{MPFA-O}$, augment I_i if $\mathcal{S}(i) \not\subseteq I_i$
  end if
  $[M_i^{\text{FC}}] \leftarrow \text{KKT}(\mathbf{c}, \mathbf{g}_j)$, $m_{ij}^{\text{FC}} \leftarrow \mathbf{c}^T \mathbf{m}_j^{i,\text{FC}}$, assemble row i of $[\mathsf{A}_p^{\text{FC}}]$ ▷ Eq. (37)
end for
solve $\{\mathcal{R}^p(p^{n+1}, S_w^{n+1})\} = 0$ for $\{p^{n+1}\}$ ▷ Eq. (48)

Algorithm 2 FC-GFDM sequential fully implicit (SFI) time stepping

Require: initial state $(\{p^0\}, \{S_w^0\})$, sources $\{q_{w,i}\}$, steps N_t, step Δt, tolerances $\varepsilon_F, \varepsilon_t$
Ensure: $(\{p^n\}, \{S_w^n\})$, $n = 1, \ldots, N_t$

for $n = 0$ **to** $N_t - 1$ **do**
  $\{p\} \leftarrow \{p^n\}$, $\{S_w\} \leftarrow \{S_w^n\}$
  repeat ▷ SFI outer loop, Fig. 1
    $\{p\} \leftarrow$ Algorithm 1$(\{S_w\})$
    $F_{ij} \leftarrow \lambda_{ij} V_i m_{ij}^{\text{FC}}(p_j - p_i)$ ▷ Eq. (49)
    for $i = 1$ **to** N **do**
      $f_{w,ij}^{\text{up}} \leftarrow f_w(S_{w,i})$ **if** $F_{ij} \geq 0$ **else** $f_w(S_{w,j})$
      solve $\mathcal{R}_i^w = 0$ for $S_{w,i}^{n+1}$ ▷ Eq. (50)
    end for
    $\{S_w\} \leftarrow \{S_w^{n+1}\}$
  until $\|\mathcal{R}^p\| < \varepsilon_F$ **and** $\|\mathcal{R}^w\| < \varepsilon_t$
  $(\{p^{n+1}\}, \{S_w^{n+1}\}) \leftarrow (\{p\}, \{S_w\})$
end for

upstream fractional flow, and $q_{w,i}$ is the water source or sink. The following algorithms succinctly describe the solution scheme.

3.4 EDFM Coupling within FC-GFDM

The EDFM formulation of Section 2.2 represents each fracture as a lower dimensional manifold embedded in the matrix continuum, and each fracture intersection as a manifold of an additional lower dimension. The matrix and fracture media are governed by their own conservation equations (5) and (6), and are coupled through the matrix-fracture exchange term and discretized through overlapping point clouds. Within each

medium, the flux-constrained operator of Section 3.3 discretizes the flow, and the matrix and fractures couple through nonneighboring connections.

Within each medium, the transmissibility between neighboring nodes is built through the flux-constrained meshless operators of Section 3.3. In a three-dimensional matrix cloud, the transmissibility is defined through the operators as in (22),

$$T_{ij} = k_{ij}\, V_i \left(m^{i,\mathrm{FC}}_{xx,j} + m^{i,\mathrm{FC}}_{yy,j} + m^{i,\mathrm{FC}}_{zz,j} \right), \tag{51}$$

where i is the matrix central node and j a neighbor inside the radius of influence, $m^{i,\mathrm{FC}}_{xx,j}$, $m^{i,\mathrm{FC}}_{yy,j}$ and $m^{i,\mathrm{FC}}_{zz,j}$ are the flux-constrained second derivative operators ∂_{xx}, ∂_{yy} and ∂_{zz} of node i, the first two being $m^{i,\mathrm{FC}}_{3j}$ and $m^{i,\mathrm{FC}}_{4j}$ of Section 2.3, k_{ij} is the harmonic average permeability of nodes i and j, and V_i is the matrix control volume. In the fracture cloud, the transmissibility is defined through the same operators,

$$T_{fg} = k_{fg}\, V_f \left(m^{f,\mathrm{FC}}_{xx,g} + m^{f,\mathrm{FC}}_{yy,g} + m^{f,\mathrm{FC}}_{zz,g} \right), \tag{52}$$

where f is the fracture central node and g a neighbor inside the radius of influence, k_{fg} is the fracture permeability, and V_f is the fracture node volume. Since the operators are truly defined in a 3D space, a tilted fracture can be handled with much ease compared to mesh-based FV counterparts.

The matrix-fracture connection between matrix node i and fracture node f is the harmonic average of the matrix and fracture half transmissibilities [22]:

$$T_{if} = \left(\frac{\langle d \rangle_{if}}{k_m\, A_{if}} + \frac{w_f}{2\, k_f\, A_{if}} \right)^{-1}, \tag{53}$$

where A_{if} is the area of the fracture plane crossing the matrix control volume Ω_i, $\langle d \rangle_{if}$ is the volume averaged normal distance from Ω_i to that plane point, w_f is the aperture, k_m is the matrix permeability, and k_f is the fracture permeability. For two distinct fracture planes that intersect, the connection is through the shared segment with the same harmonic average:

$$T_{f_1 f_2} = \left(\frac{\langle d \rangle_{f_1}}{k_{f_1}\, w_{f_1}\, L_{f_1 f_2}} + \frac{\langle d \rangle_{f_2}}{k_{f_2}\, w_{f_2}\, L_{f_1 f_2}} \right)^{-1} = \frac{L_{f_1 f_2}}{\dfrac{\langle d \rangle_{f_1}}{k_{f_1}\, w_{f_1}} + \dfrac{\langle d \rangle_{f_2}}{k_{f_2}\, w_{f_2}}}, \tag{54}$$

where $L_{f_1 f_2}$ is the length of the intersection segment shared by F_1 and F_2, w_{f_1} and w_{f_2} are the apertures and k_{f_1} and k_{f_2} the permeabilities of fracture planes F_1 and F_2, respectively, and $\langle d \rangle_{f_1}$ and $\langle d \rangle_{f_2}$ are the average normal distances from nodes f_1 and f_2 , respectively, to the intersection line.

The nonneighboring fluxes are appended without altering the flux-constrained stencil: each node adds the flux across its nonneighboring connections to the conservative balance (48), with the transmissibility taken from (53) or (54). Assembling both matrix

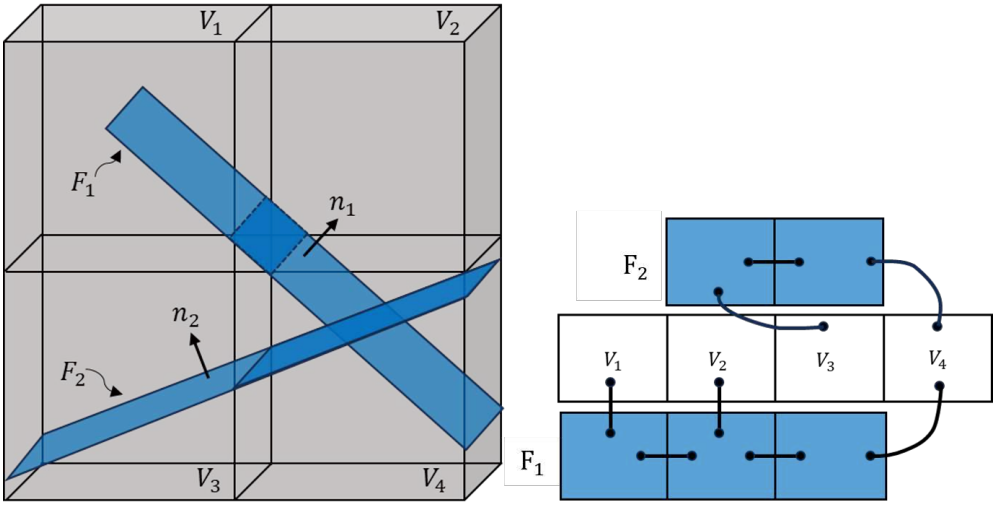


Fig. 7 Nonneighboring connection types in the EDFM formulation. Left: fractures F_1 and F_2 crossing the matrix cells V_1–V_4 with interface normals $\mathbf{n}_1, \mathbf{n}_2$. Right: the resulting matrix-fracture and fracture intersection connections. Adapted from Poli et al. [29].

and fracture clouds results in the coupled system

$$\begin{pmatrix} [A_{mm}] & [A_{mf}] \\ [A_{mf}]^T & [A_{ff}] \end{pmatrix} \begin{pmatrix} \{p_m\} \\ \{p_f\} \end{pmatrix} = \begin{pmatrix} \{Q_m\} \\ \{Q_f\} \end{pmatrix}, \tag{55}$$

where the diagonal block $[A_{mm}]$ assembles the matrix transmissibilities (51), $[A_{ff}]$ the fracture transmissibilities (52) augmented by the intersection transmissibilities (54), the off diagonal block $[A_{mf}]$ the matrix-fracture transmissibilities (53), and $\{p_m\}$, $\{p_f\}$ and $\{Q_m\}$, $\{Q_f\}$ collect the matrix and fracture pressures and sources, respectively.

4 Numerical Experiments and Discussion

In this section, our FC-GFDM is assessed through a sequence of numerical setups of different physical and geometric conditions. Throughout, the Matlab Reservoir Simulation Toolbox (MRST) [30] is used to provide counterpart mesh-based FV reference solutions to compare against. Test Case 1 verifies that the Flux-Constrained meshless operator reproduces the single phase problem of the target finite volume method scheme, namely the TPFA method. Test Case 2 presents the MPFA-O method with full tensor permeability, and Test Case 3 presents nonorthogonal and irregular clouds with the FC-GFDM–MPFA-O. Test Case 4 deals with two-phase transport problems in 2D and 3D. Finally, Test Case 5 presents the fracture setups.

4.1 Test Case 1: single phase flow problem

In this example, we solve the incompressible pressure equation (2) on a homogeneous, isotropic domain with properties given in Table 1.

Table 1 Geometric, petrophysical, and discretization parameters for Test Case 1.

Parameter	Value	Unit
Domain size $L_x \times L_y$	100×100	m
Reservoir thickness h_z	10	m
Characteristic spacing h	5	m
Matrix permeability k	100 (9.87×10^{-14})	mD (m^2)
Matrix porosity ϕ	0.1	–
Fluid viscosity μ	2.0	cP
Support radius parameter β	1.5	–
Support radius $r_m = \beta h$	7.5	m
Dual cell mode	PEBI	–
Finite volume reference	MRST (TPFA)	–

Flow is driven horizontally by Dirichlet conditions on the lateral boundaries, $p = 14$ MPa on the left and $p = 7$ MPa on the right, and no-flow conditions on the top and bottom boundaries. The meshless solution uses a regular cloud of $21 \times 21 = 441$ nodes with the PEBI dual cell and the TPFA constraint with $\mathbf{c}^{TPFA} = [0, 0, 1, 1, 0]^T$. The MRST reference solution was obtained using the `incompTPFA` solver on the 20×20 Cartesian grid. Because the cloud is regular, the PEBI interfaces are face orthogonal and the two-point flux is $O(h^2)$-consistent.

Figure 8 compares the incidence matrices of GFDM, FC-GFDM, and MRST. Note that the matrices are cropped to a size of 65×65 to enhance structure visibility. The conventional GFDM with the same support radius constructs a stencil with a nine-point footprint (nnz = 3721). Our FC-GFDM folds this onto the geometric neighbors $\mathcal{N}(i) \cup \{i\}$, and yields the usual five point stencil of a finite volume operator (nnz = 2121); the MRST TPFA reference results in nnz = 1920. The small difference in nnz between FC-GFDM and TPFA is a result of the boundary nodes. The node cloud in FC-GFDM wraps the domain from boundary to boundary with 441 nodes while TPFA-FV is a cell-centered formulation with 400 cells in this example.

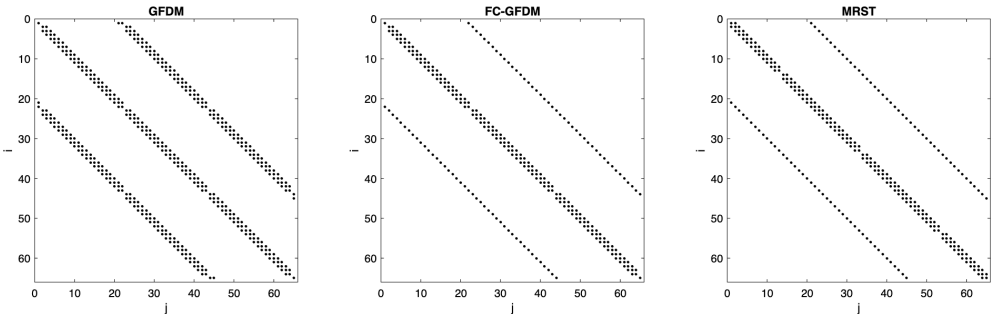


Fig. 8 Sparsity Matrices, Left: standard GFDM; middle: FC-GFDM–TPFA; right: MRST TPFA .

Figure 9 compares the absolute difference in the pressure results. As can be seen, the FC-GFDM pressure solution agrees remarkably well with the MRST results with a maximum absolute difference of $\max|\Delta p| = 5.599 \times 10^{-5}$ psia ($\approx 3 \times 10^{-8}$ relative) at the boundaries.

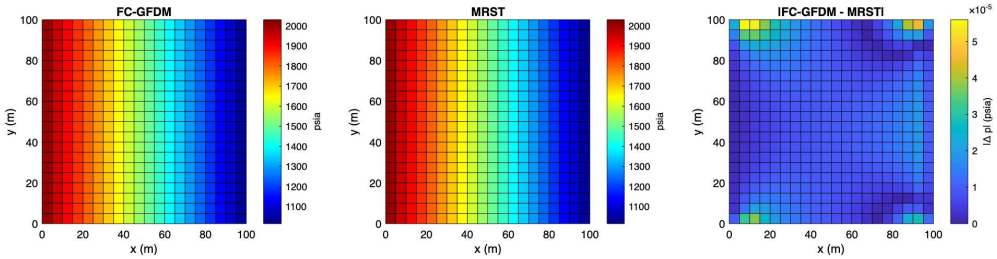


Fig. 9 Single phase pressure on the 100×100 m domain. Left: FC-GFDM–TPFA; middle: MRST TPFA; right: pointwise difference ($\max|\Delta p| = 5.599 \times 10^{-5}$ psia, $\approx 3 \times 10^{-8}$ relative), confined to the boundary cells.

4.2 Test Case 2: full tensor permeability

This test case demonstrates our FC-GFDM MPFA method for modeling tensorial flow on regular grids. A full permeability tensor whose principal axes are rotated relative to the point cloud is applied:

$$\boldsymbol{K} = \mathbf{R}(\theta)\,\mathrm{diag}(k_1, k_2)\,\mathbf{R}(\theta)^T, \qquad \mathbf{R}(\theta) = \begin{bmatrix} \cos\theta & -\sin\theta \\ \sin\theta & \cos\theta \end{bmatrix}, \tag{56}$$

where k_1 and k_2 are the principal permeability values, $\mathbf{R}(\theta)$ is the rotation matrix, and θ is the rotation angle.

Figure 10 depicts the pressure solution with $k_1 = 100$ mD, $k_2 = 10$ mD, and $\theta = 30°$, for TPFA, MPFA-O, and our FC-GFDM. As in the previous case, our FC-GFDM result is indistinguishable from its MRST MPFA-O counterpart.

4.3 Test Case 3: nonorthogonal and irregular clouds

In this example, we showcase nonorthogonality and irregular clouds by perturbing the interior nodes of the regular spacing so that the consistency of the meshless operator is examined.

Figure 11 shows the pressure profiles for regular and 30% irregular clouds, compared against MRST MPFA-O reference solutions, for both isotropic and full tensor permeability. As can be seen, our FC-GFDM solutions match those of the MRST reference solutions. This example demonstrates our formulation's ability to handle nonorthogonal irregular point clouds via the MPFA-O flux constraint. Alternative flux constraints (e.g., MPFA variants) for more complex geometries and highly unstructured grids can certainly be embedded in the FC-GFDM formulation.

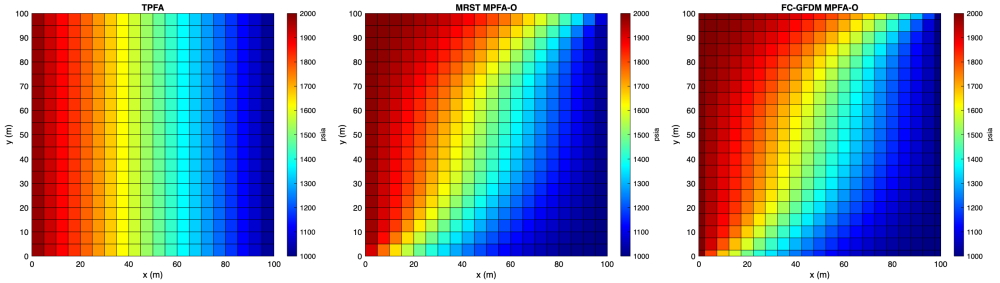


Fig. 10 Pressure fields for the full tensor case on a regular grid ($k_1 = 100$ mD, $k_2 = 10$ mD, $\theta = 30°$). Left: TPFA; center: MRST MPFA-O; right: FC-GFDM MPFA-O.

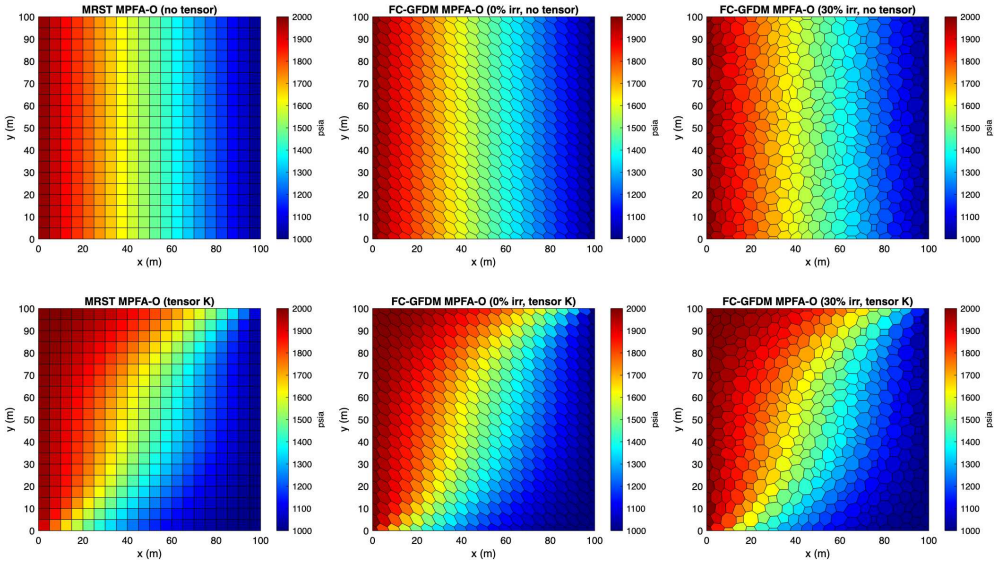


Fig. 11 FC-GFDM and MRST MPFA-O pressure on the regular and 30% irregular clouds ($k_1 = 100$ mD, $k_2 = 10$ mD, $\theta = 30°$ for the tensor case). Top row with isotropic permeability; bottom row with full tensor permeability. Left: MRST MPFA-O; center: FC-GFDM 0% irregular; right: FC-GFDM 30% irregular.

4.4 Test Case 4: two-phase transport in 2D and 3D

Here, we solve the transport problem in a 2D and 3D setting, showcasing local mass conservation as the saturation front advances. Fluid, rock, well, and discretization data are given in Table 2.

Figure 12 shows the water saturation at 0.60 pore volume injected. Water enters at the injector (blue triangle) on the left and displaces oil toward the producer on the right (red triangle), and the swept region forms a front that departs from the horizontal line between the wells, following the principal anisotropy direction. The three

Table 2 Geometric, petrophysical, and discretization parameters for Test Case 4.

Parameter	Value	Unit
Reservoir and discretization data		
Domain size $L_x \times L_y$	100×100	m
Reservoir thickness h_z	10	m
Characteristic spacing h	5	m
FC-GFDM nodes $n_x \times n_y$	21×21	–
Principal permeabilities k_1, k_2	100, 10	mD
Permeability rotation angle θ	60	$^\circ$
Matrix porosity ϕ	0.20	–
Support radius parameter β	2.0	–
Support radius $r_m = \beta h$	10	m
Dual cell mode	centroid	–
Maximum node irregularity	30	%
Fluid and rock data		
Water viscosity μ_w	0.5	cP
Oil viscosity μ_o	2.0	cP
Connate water S_{wc}	0.0	–
Residual oil S_{or}	0.0	–
Corey exponents $n_w = n_o$	2.0	–
Endpoint $k_{rw}^{\max} = k_{ro}^{\max}$	1.0	–
Initial water saturation S_w^0	0.0	–
Well and operating data		
Water injection rate q_{inj}	2×10^{-4}	m^3/s
Producer BHP	8 (1160)	MPa (psia)
Wellbore radius r_w	0.10	m
Pore volumes injected (PVI)	0.60	–

discretizations agree: the FC-GFDM solutions on the regular and the 30% irregular cloud reproduce the swept region and the front position of the MRST reference solution.

Figure 13 extends the displacement to 3D at 0.40 pore volume injected, again on centroid dual cells, comparing the MRST reference solution with those of FC-GFDM on regular and 30% irregular 3D clouds. It can be seen that the three solutions agree on the extent and shape of the swept region, confirming both consistency and local conservation of FC-GFDM for 3D, regular or irregular, point clouds.

4.5 Test Case 5: fractured reservoir via EDFM

In this final example, we simulate a fractured reservoir using the EDFM framework. To showcase the geometric versatility of the meshless discretization, the same network is built in two configurations: Figure 14 shows the nontilted arrangement with vertical fractures, and Figure 15 shows the tilted arrangement with most of the fractures dipping out of the vertical plane.

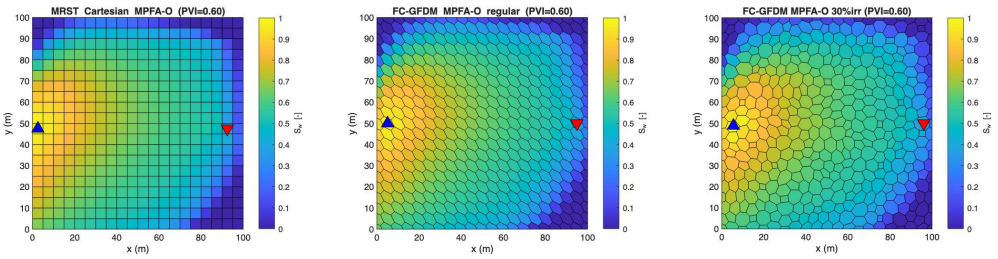


Fig. 12 Water saturation at 0.60 pore volume injected. Left: MRST Cartesian; center: FC-GFDM regular cloud; right: FC-GFDM 30% irregular cloud.

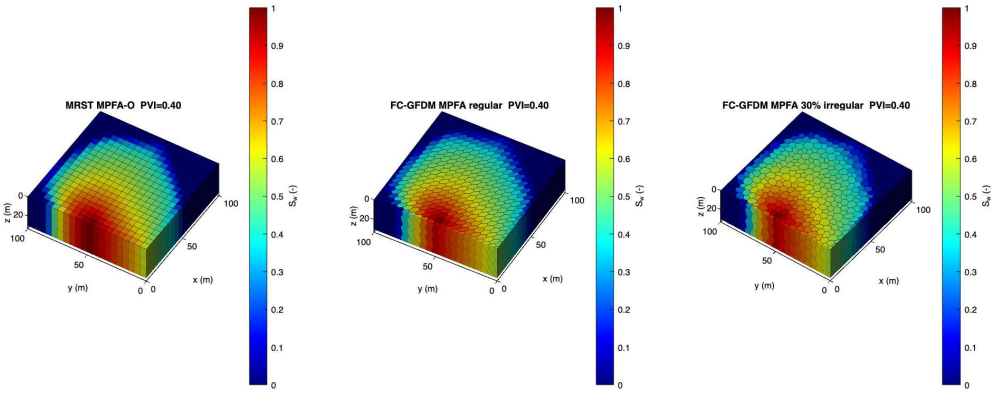


Fig. 13 Three-dimensional water saturation at 0.40 pore volume injected on centroid dual cells. Left: MRST MPFA-O; center: FC-GFDM regular cloud; right: FC-GFDM 30% irregular cloud.

The rotation-invariant nature of the meshless operators eliminates directional bias in coupling calculations and significantly simplifies the handling of arbitrarily oriented and intersecting fractures. We exploit this property in the tilted configuration studied here, in which fractures of different orientation, length, and position are simulated through an injector to producer pair. Table 3 lists the geometry and simulation parameters used in the example.

Figure 16 shows the FC-GFDM and MRST pressure profiles along with the absolute pressure difference plot. The two are qualitatively indistinguishable with an absolute difference peaking at 15.1 psia confined near the well cells.

Figure 17 shows the FC-GFDM and MRST water saturation maps at 250 days and the absolute saturation difference. We also observe that the two fields are visually indistinguishable. However, there are some minor differences that we attribute to the calculation of the average distance to the fracture nodes between both methods.

Figure 18 shows the FC-GFDM water saturation evolution at different snapshots.

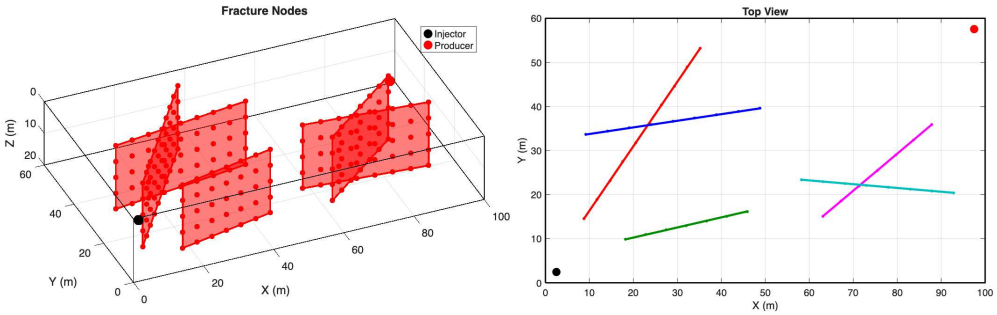


Fig. 14 Nontilted fracture network. Left: 3D fracture nodes; right: top view.

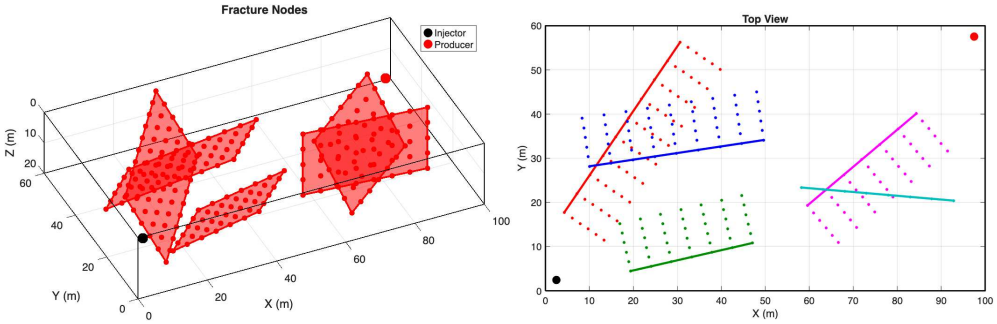


Fig. 15 Tilted fracture network. Left: 3D fracture nodes; right: top view.

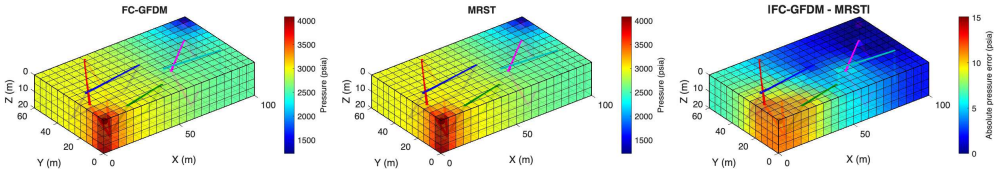


Fig. 16 Pressure in the tilted fractured reservoir. Left: FC-GFDM pressure solution; center: MRST pressure solution; right: absolute difference.

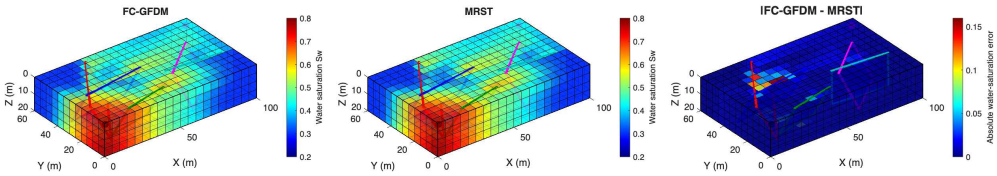


Fig. 17 Water saturation in the tilted fractured reservoir. Left: FC-GFDM water saturation; center: MRST water saturation; right: absolute difference.

Table 3 Simulation parameters for the fractured reservoir test case.

Parameter	Value	Unit
Reservoir data		
Domain $L_x \times L_y \times L_z$	$100 \times 60 \times 20$	m
Matrix grid $n_x \times n_y \times n_z$	$20 \times 12 \times 4$	–
Support radius parameter β	1.8	–
Matrix permeability k_m	1	mD
Matrix porosity ϕ_m	0.10	–
Fracture permeability k_f	10 000	mD
Fracture aperture w_f	0.009	m
Fracture porosity ϕ_f	0.30	–
Water viscosity μ_w	0.5	cP
Oil viscosity μ_o	2.0	cP
Connate water S_{wc}	0.20	–
Residual oil S_{or}	0.20	–
Corey exponents $n_w = n_o$	2.0	–
Endpoint $k_{rw}^{\max} = k_{ro}^{\max}$	0.80	–
Initial water saturation S_w^0	0.30	–
Production and injection well data		
Water injection rate	65	bbl/d
Producer BHP	1000	psia
Total time	250	day

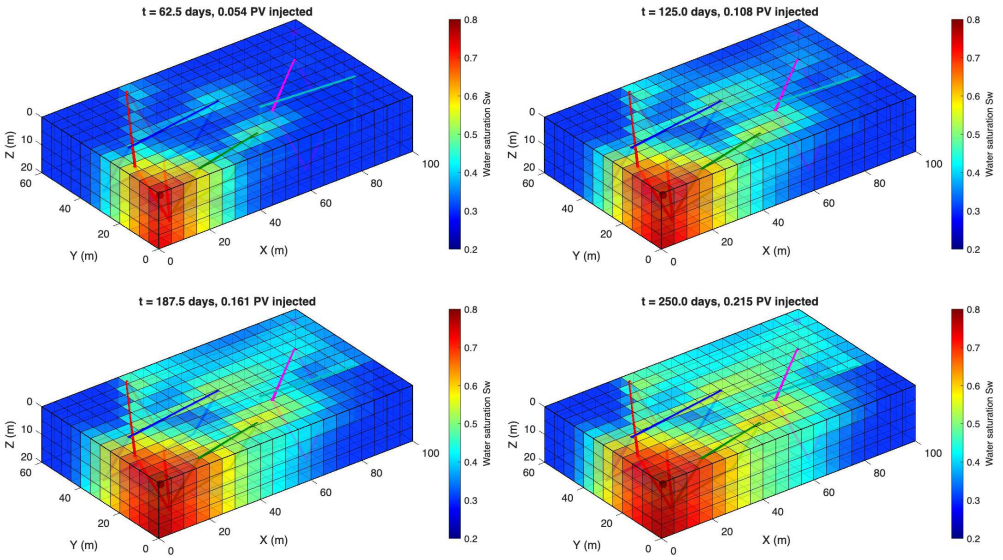


Fig. 18 FC-GFDM water saturation maps at 62.5, 125, 187.5, and 250 days.

5 Conclusions

In this work, we developed a flux-constrained generalized finite difference method (FC-GFDM), a first-of-its-kind meshless scheme that enforces strict local mass conservation for Eulerian reservoir simulation on arbitrary point clouds. The proposed formulation recovers local conservation by augmenting the weighted least squares Taylor system with a K-K-T flux balance constraint derived from a target finite volume stencil, so that each operator simultaneously satisfies discrete flux balance and Taylor consistency. For typical 2D settings, our method folds the traditional nine-point GFDM footprint onto a five-point stencil. Dual cells, PEBI or centroidal, are built locally on regular or irregular point clouds without a global mesh. Both two-point (TPFA) and multipoint, namely (MPFA-O), discrete fluxes were implemented in our FC-GFDM, with the latter restoring consistency for full permeability tensors and non-K-orthogonal settings. Moreover, the rotation-invariant meshless operators allow for the ease of handling fracture planes in arbitrarily oriented and tilted angles directly in three-dimensional space.

Verification against MRST finite volume references was carried out across different test scenarios. For flow problems, FC-GFDM–TPFA reproduced the reference solution to an absolute difference of the order 1×10^{-5} psia. For tensorial flow, our FC-GFDM-MPFA-O captured the rotated pressure field, indistinguishable from the MRST reference solution, on both regular and irregular point clouds. The property of local conservation was shown through the two-phase transport setups, where the swept region and front position matched the reference in two and three dimensions, and for regular and irregular clouds with tensorial effects. Finally, we applied FC-GFDM to a complex tilted fracture network with the EDFM framework and matched the MRST reference solution for pressure and water saturation.

A Derivation of the KKT System

The flux-constrained operator solves the constrained weighted least squares problem posed in Section 3.2: the weighted Taylor residual (consistency (32) and minimum weighted norm (34)) is minimized subject to the flux conservation constraint (33),

$$\min_{\mathbf{m}} \ \tfrac{1}{2}\left\|[W]^{-1}([X]\mathbf{m}-\boldsymbol{\phi})\right\|^2, \qquad \mathbf{c}^T\mathbf{m} = C_{\text{flux}}. \tag{A.1}$$

Here $[X]$ (10) is the Taylor basis matrix, $[W]$ (14) the diagonal weight matrix, $\mathbf{m} \in \mathbb{R}^5$ the derivative vector $[\partial_x p,\, \partial_y p,\, \partial_{xx} p,\, \partial_{yy} p,\, \partial_{xy} p]^T$, $\boldsymbol{\phi}$ the pressure differences (11), $\mathbf{c} = (0, 0, 1, 1, 0)^T$ the vector selecting the Laplacian $\partial_{xx} p + \partial_{yy} p$, and C_{flux} the flux derived coefficient (35) enforcing conservation. Section 3.2 assembles the per node operator one neighbor column at a time; the derivation below solves this system for a single right hand side $\boldsymbol{\phi}$, and its column form (37) is recovered by setting $\boldsymbol{\phi} = \mathbf{e}_j$ and $C_{\text{flux}} = g_j$.

Introducing the multiplier μ, the Lagrangian combines the objective with the constraint,

$$\mathcal{L}(\mathbf{m},\mu) = \tfrac{1}{2}([X]\mathbf{m}-\boldsymbol{\phi})^T[W]([X]\mathbf{m}-\boldsymbol{\phi}) + \mu\big(\mathbf{c}^T\mathbf{m} - C_{\text{flux}}\big), \tag{A.2}$$

which on expanding the quadratic term reads

$$\mathcal{L} = \tfrac{1}{2}\big[\mathbf{m}^T[X]^T[W][X]\mathbf{m} - 2\boldsymbol{\phi}^T[W][X]\mathbf{m} + \boldsymbol{\phi}^T[W]\boldsymbol{\phi}\big] + \mu\big(\mathbf{c}^T\mathbf{m} - C_{\text{flux}}\big). \tag{A.3}$$

Setting $\partial\mathcal{L}/\partial\mathbf{m} = \mathbf{0}$ gives

$$[X]^T[W][X]\mathbf{m} - [X]^T[W]\boldsymbol{\phi} + \mu\mathbf{c} = \mathbf{0} \quad\Longrightarrow\quad [X]^T[W][X]\mathbf{m} + \mu\mathbf{c} = [X]^T[W]\boldsymbol{\phi}, \tag{A.4}$$

while $\partial\mathcal{L}/\partial\mu = 0$ recovers the constraint

$$\mathbf{c}^T\mathbf{m} - C_{\text{flux}} = 0. \tag{A.5}$$

Combining (A.4) and (A.5) into matrix form, and writing $[A] = [X]^T[W][X]$, the weighted Gram matrix of Eq. (15), and $\mathbf{b} = [X]^T[W]\boldsymbol{\phi}$, yields the $(5{+}1)\times(5{+}1)$ KKT system

$$\begin{pmatrix} [A] & \mathbf{c} \\ \mathbf{c}^T & 0 \end{pmatrix}\begin{pmatrix} \mathbf{m} \\ \mu \end{pmatrix} = \begin{pmatrix} \mathbf{b} \\ C_{\text{flux}} \end{pmatrix}. \tag{A.6}$$

From the first block equation $[A]\mathbf{m} + \mu\mathbf{c} = \mathbf{b}$,

$$\mathbf{m} = [A]^{-1}(\mathbf{b} - \mu\mathbf{c}) = [A]^{-1}\mathbf{b} - \mu[A]^{-1}\mathbf{c}, \tag{A.7}$$

and substituting into the constraint $\mathbf{c}^T\mathbf{m} = C_{\text{flux}}$ gives $\mathbf{c}^T[A]^{-1}\mathbf{b} - \mu\,\mathbf{c}^T[A]^{-1}\mathbf{c} = C_{\text{flux}}$, hence

$$\mu = \frac{\mathbf{c}^T[A]^{-1}\mathbf{b} - C_{\text{flux}}}{\mathbf{c}^T[A]^{-1}\mathbf{c}}. \tag{A.8}$$

Defining the positive scalar $\gamma = \mathbf{c}^T[A]^{-1}\mathbf{c}$, the γ_i of Eq. (38), and substituting (A.8) into (A.7),

$$\mathbf{m} = \underbrace{[A]^{-1}\mathbf{b}}_{\mathbf{m}_{\text{unc}}} - \frac{1}{\gamma}[A]^{-1}\mathbf{c}\big(\mathbf{c}^T[A]^{-1}\mathbf{b} - C_{\text{flux}}\big). \tag{A.9}$$

Writing $\mathbf{m}_{\text{unc}} = [A]^{-1}\mathbf{b}$ for the unconstrained solution gives

$$\mathbf{m} = \mathbf{m}_{\text{unc}} - \frac{1}{\gamma}[A]^{-1}\mathbf{c}\big(\mathbf{c}^T\mathbf{m}_{\text{unc}} - C_{\text{flux}}\big). \tag{A.10}$$

The correction term computes the flux imbalance $\mathbf{c}^T\mathbf{m}_{\text{unc}} - C_{\text{flux}}$ of the unconstrained gradient, adjusts $\mathbf{m}$ in the direction $[A]^{-1}\mathbf{c}$, and scales by $1/\gamma$ to satisfy conservation exactly, so the row sum of the discrete Laplacian coefficients vanishes. This furnishes the KKT system (37) and the flux-constrained operator (38) of Section 3.2; solving it for each basis vector $\boldsymbol{\phi} = \mathbf{e}_j$ assembles the operator $[M_i^{\text{FC}}]$ (39) column by column.

References

[1] J. E. Warren and P. J. Root. The behavior of naturally fractured reservoirs. *Society of Petroleum Engineers Journal*, 3(03):245–255, 1963.

[2] H. Kazemi, L. S. Merrill Jr., K. L. Porterfield, and P. R. Zeman. Numerical simulation of water-oil flow in naturally fractured reservoirs. *Society of Petroleum Engineers Journal*, 16(06):317–326, 1976.

[3] K. Pruess and T. N. Narasimhan. A practical method for modeling fluid and heat flow in fractured porous media. *Society of Petroleum Engineers Journal*, 25(01):14–26, 1985.

[4] Y. S. Wu and K. Pruess. A multiple-porosity method for simulation of naturally fractured petroleum reservoirs. *SPE Reservoir Engineering*, 3(01):327–336, 1988.

[5] M. Karimi-Fard, L. J. Durlofsky, and K. Aziz. An efficient discrete-fracture model applicable for general-purpose reservoir simulators. *SPE Journal*, 9(02):227–236, 2004.

[6] S. H. Lee, M. A. Lough, and C. L. Jensen. Hierarchical modeling of flow in naturally fractured formations with multiple length scales. *Water Resources Research*, 37(3):443–455, 2001.

[7] A. Moinfar, A. Varavei, K. Sepehrnoori, and R. T. Johns. Development of an efficient embedded discrete fracture model for 3D compositional reservoir simulation in fractured reservoirs. *SPE Journal*, 19(2):289–303, 2014.

[8] M. Tęne, S. B. Bosma, M. S. Al Kobaisi, and H. Hajibeygi. Projection-based embedded discrete fracture model (pEDFM). *Advances in Water Resources*, 105:205–216, 2017.

[9] K. H. Coats, R. L. Nielsen, M. H. Terhune, and A. G. Weber. Simulation of three-dimensional, two-phase flow in oil and gas reservoirs. *Society of Petroleum Engineers Journal*, 7(4):377–388, 1967.

[10] C. L. McMichael and G. W. Thomas. Reservoir simulation by Galerkin's method. *Society of Petroleum Engineers Journal*, 13(3):125–138, 1973.

[11] T. Y. Hou and X.-H. Wu. A multiscale finite element method for elliptic problems in composite materials and porous media. *Journal of Computational Physics*, 134(1):169–189, 1997.

[12] M. F. Wheeler and I. Yotov. A multipoint flux mixed finite element method. *SIAM Journal on Numerical Analysis*, 44(5):2082–2106, 2006.

[13] R. A. Klausen and T. F. Russell. Relationships among some locally conservative discretization methods which handle discontinuous coefficients. *Computational*

Geosciences, 8(4):341–377, 2004.

[14] K. Aziz and A. Settari. *Petroleum Reservoir Simulation*. Applied Science Publishers, London, 1979.

[15] I. Aavatsmark, T. Barkve, Ø. Bøe, and T. Mannseth. Discretization on non-orthogonal, quadrilateral grids for inhomogeneous, anisotropic media. *Journal of Computational Physics*, 127(1):2–14, 1996.

[16] M. G. Edwards and C. F. Rogers. Finite volume discretization with imposed flux continuity for the general tensor pressure equation. *Computational Geosciences*, 2(4):259–290, 1998.

[17] P. S. Jensen. Finite difference techniques for variable grids. *Computers & Structures*, 2(1-2):17–29, 1972.

[18] T. Liszka and J. Orkisz. The finite difference method at arbitrary irregular grids and its application in applied mechanics. *Computers & Structures*, 11(1-2):83–95, 1980.

[19] J. J. Benito, F. Ureña, and L. Gavete. Influence of several factors in the generalized finite difference method. *Applied Mathematical Modelling*, 25(12):1039–1053, 2001.

[20] L. Gavete, M. L. Gavete, and J. Benito. Improvements of generalized finite difference method and comparison with other meshless method. *Applied Mathematical Modelling*, 27(10):831–847, 2003.

[21] X. Rao, Y. Liu, and H. Zhao. An upwind generalized finite difference method for meshless solution of two-phase porous flow equations. *Engineering Analysis with Boundary Elements*, 137:105–118, 2022.

[22] X. Rao, L. Cheng, R. Cao, P. Jia, and Y.-S. Wu. A meshless numerical modeling method for fractured reservoirs based on extended finite volume method. *SPE Journal*, 27(6):3525–3556, 2022.

[23] E. K.-Y. Chiu, Q. Wang, R. Hu, and A. Jameson. A conservative mesh-free scheme and generalized framework for conservation laws. *SIAM Journal on Scientific Computing*, 34(6):A2896–A2916, 2012.

[24] P. Suchde, J. Kuhnert, S. Schröder, and A. Klar. A flux conserving meshfree method for conservation laws. *International Journal for Numerical Methods in Engineering*, 112(3):238–256, 2017.

[25] W. Karush. Minima of functions of several variables with inequalities as side constraints. M.Sc. dissertation, Department of Mathematics, University of Chicago, Chicago, IL, 1939.

[26] H. W. Kuhn and A. W. Tucker. Nonlinear programming. In *Proceedings of the Second Berkeley Symposium on Mathematical Statistics and Probability*, pages 481–492. University of California Press, Berkeley, CA, 1951.

[27] P. Suchde. *Conservation and Accuracy in Meshfree Generalized Finite Difference Methods*. Fraunhofer Verlag, Kaiserslautern, 2018.

[28] I. Aavatsmark. An introduction to multipoint flux approximations for quadrilateral grids. *Computational Geosciences*, 6:405–432, 2002.

[29] R. E. B. Poli, M. V. B. Machado, and K. Sepehrnoori. Advancements and perspectives in embedded discrete fracture models (EDFM). *Energies*, 17(14):3550, 2024.

[30] K.-A. Lie. *An Introduction to Reservoir Simulation Using MATLAB/GNU Octave: User Guide for the MATLAB Reservoir Simulation Toolbox (MRST)*. Cambridge University Press, Cambridge, 2019.